Journal of Molecular Catalysis A: Chemical 379 (2013) 152–162

Contents lists available at ScienceDirect

Journal of Molecular Catalysis A: Chemical

journal homepage: www.elsevier.com/locate/molcata

# Microwave assisted efficient protocol for the classic Ullmann homocoupling reaction using Cu–Mg–Al hydrotalcite catalysts

Katabathini Narasimharao[a,*], Ebtisam Al-Sabban[a], Tamer S. Saleh[a], Ainara Garcia Gallastegui[b,c], Almudena Celaya Sanfiz[b,c], Sulaiman Basahel[a], Shaeel Al-Thabaiti[a], Abdulrahman Alyoubi[a], Abdullah Obaid[a], Mohamed Mokhtar[a,*]

[a] Department of Chemistry, Faculty of Science, King Abdulaziz University, P.O. Box 80203, Jeddah 21589, Saudi Arabia
[b] Department of Chemistry, Imperial College London, London SW7 2AZ, UK
[c] Bio Nano Consulting, 338 Euston Road, London NW1 3BT, UK

ARTICLE INFO

*Article history:*
Received 13 June 2013
Received in revised form 9 August 2013
Accepted 12 August 2013
Available online xxx

*Keywords:*
Ullmann homocoupling
Iodobenzene
Aryl halides
Cu–Mg–Al hydrotalcites
Microwave irradiation

ABSTRACT

Four hydrotalcite catalysts containing different amounts of Cu and Mg cations, with varying atomic ratios of Cu:Mg:Al in the brucite-like layers of 0:2:1, 0.5:1.5:1, 1:1:1 and 2:0:1, were prepared by co-precipitation method. The synthesized catalysts were tested for classic Ullmann homocoupling of iodobenzene to produce biphenyl without using any stoichiometric amounts of base or reducing agent. The Mg–Al hydrotalcite catalyst without Cu ions is inactive, but the doping of Cu ions (Cu/Al = 0.5) into the Mg–Al hydrotalcite framework led to 63% conversion of iodobenzene under microwave irradiation. Gradual increase of Cu content and concomitant decrease of Mg content resulted in an increase in the conversion of iodobenzene and selectivity to biphenyl. The physico-chemical properties of hydrotalcite catalysts were studied by chemical analysis, XRD, FTIR, $N_2$-physisorption, SEM, XPS, ESR and TPR techniques to understand the state of Cu ions presented in the hydrotalcite framework. It appears that presence of easily reducible isolated $Cu^{2+}$ ions is essential to obtain improved performance of the catalyst.



## 1. Introduction

Numerous attempts have been made to develop heterogeneous catalysts for C—C bond-forming reactions because of their increasing importance in pharmaceutical, agrochemical and fine chemical industries [1–4]. The synthesis and utilization of biaryls is interesting because biaryls can be used as monomers for the synthesis of conductive polymers [5–7], natural products such as, steganone [8] and receptrice macrocyclic molecules [9]. There are many methods to synthesize symmetrical biaryls; one of the main routes is the classic Ullmann coupling reaction. Although the Ullmann reaction is over 100 years old, it is still used in industry today. Conventionally, the Ullmann coupling reaction (Scheme 1) is carried out at high temperatures (125–300 °C) in the presence of base such as NaOt-Bu [10], $Cs_2CO_3$ [11], $K_2CO_3$ [12] and $K_3PO_4$ [13]. In addition, these reactions often require the use of stoichiometric amounts of copper reagents [copper powder or copper(I) salt and copper(I) thiophene-2-carboxylate], which result in the production of undesirable chemical waste [4].

The homogenous catalytic methodologies reported in the literature suffer from disadvantages, such as disposal of waste and difficulty in recovering the catalyst from the products. In the last decade, there were notable improvements in the development of heterogeneous catalyst for Ullmann coupling reaction for synthesis of biaryl [14].

Wan et al. [15] synthesized Pd deposited hybrid mesoporous periodic organosilicas (Ph-MCM-41) with phenylene moieties embedded inside the silica and used these materials as a heterogeneous catalyst for the Ullmann coupling reaction in water. They observed 75.4% iodobenzene conversion after 10 h at 100 °C with 98% selectivity to biphenyl. However, Pd based catalysts are air sensitive, expensive and require an additional reducing agent, thus limit their relevance for industrial applications [16].

Due to these disadvantages associated with Pd based catalysts, many researchers have begun to reinvestigate Cu based catalysts; Miao and Wang [17] developed alternative approaches to the classic Ullmann reaction of C—C formation using functionalized silica-gel immobilized Cu(II) catalyst. However, irreversible binding of metal ions and lack of selectivity are the main disadvantages of silica bound ligands [18]. Ponce and Klabunde [19]

* Corresponding authors. Tel.: +966 500558045; fax: +966 26952292.
*E-mail addresses:* katabathini@yahoo.com (K. Narasimharao), mmokhtar2000@yahoo.com (M. Mokhtar).

1381-1169/$ – see front matter © 2013 Elsevier B.V. All rights reserved.
http://dx.doi.org/10.1016/j.molcata.2013.08.013

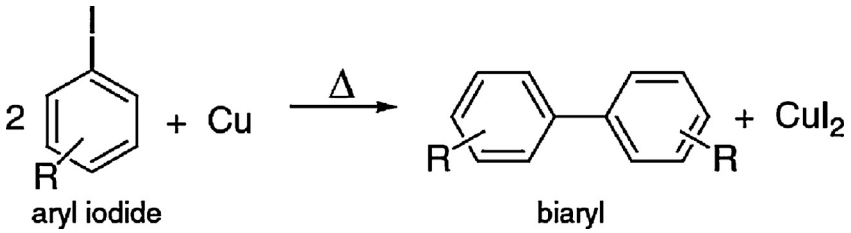


**Scheme 1.** The classic Ullmann reaction for coupling of aryl iodides by reaction with copper metal at high temperature.

synthesized nanocrystalline particles of copper and their catalytic reactivity have been tested in the Ullman homocoupling. The authors observed maximum biphenyl yield of 90% at 150 °C after 6 h for the Cu nanoparticle sample and toluene as a solvent. Samim et al. [20] studied effect of size of Cu nanoparticles in the conversion and yield in the Ullmann coupling reaction. They observed a drastic change in the yield of biphenyl from 43% to 95% when they switched the catalyst from micro size Cu particles to nano size (8 nm) Cu particles. Unfortunately, most of the Cu based catalysts need an extra base [21,22] in sub-stoichiometric amounts and/or require long reaction times [23]. More recently, Li et al. [24] reported for the first time the application of gold cluster supported catalysts [$Au_{25}(SR)_{18}/CeO_2$] for an Ullmann homocoupling reaction of aryl iodides. The catalyst was found to give a 99.8% yield, using conventional heating, 48 h reaction time with iodobenzene and excellent recyclability, however this gold nano-cluster catalyst is expensive, needs extra base and also has low thermal stability. Hence, it is of great practical interest to develop an efficient, inexpensive, solid heterogeneous catalyst that can catalyze the Ullmann coupling of iodoaryls to biaryls in the absence of base, with short reaction times yielding a high amount of product, which can be easily separated and reused in the reaction several times.

Mg–Al hydrotalcites (HT) and mixed oxides derived from hydrotalcite precursors are widely used catalysts for various chemical reactions because they are relatively cheap, do not contain any toxic metals and are stable at high temperatures in polar and non-polar reaction conditions [25]. Leon et al. [26] reported that the basic properties of these materials are dependent on chemical composition and synthesis procedure used. On the other hand, properties such as presence of basic sites, the nature of basic sites, their density, type of solvent, largely affects its performance in different reactions, since the chemical reactions involve a complex sequence of elemental steps catalyzed by active sites. Auer et al. [27] used mixed-metal oxides, derived from Cu–Mg–Al hydroxy carbonates, for the synthesis of methyl amines and observed maximum activity with a composite that possessed a hydrotalcite like structure. Iwai et al. [28] successfully used an alkali-promoted Cu–Mg–Al hydrotalcite catalyst for selective oxidation of 2,6-di-*tert*-butylphenol. The authors also claimed that presence of $Cu^{2+}$ ions is essential to obtain improved catalytic performance.

Motivated by the aforementioned findings, and in continuation of our research interest in the use of hydrotalcite catalysts for organic transformations [29], "Microwave induced Organic Reaction Enhancement" (MORE) chemistry has been utilized for rapid synthesis of biaryl molecules. Here, we report a new, simple protocol that does not require any reducing agent or additional base via recyclable solid Cu–Mg–Al and/or Cu–Al hydrotalcite catalyst for synthesis of biaryl. To the best of our knowledge, the application of Cu–Mg–Al based hydrotalcite catalysts for this reaction has not previously been reported. A detailed characterization of catalysts has been carried out to understand how the Cu ions in hydrotalcite structure influence the reaction mechanism.

## 2. Experimental

### 2.1. Preparation of catalysts

MgLDH (Cu:Mg:Al = 0:2:1), CuLDH-1 (Cu:Mg:Al = 0.5:1.5:1), CuLDH-2 (Cu:Mg:Al = 1:1:1) and CuLDH-3 (Cu:Mg:Al = 2:0:1) materials were prepared by a co-precipitation method. Two solutions, namely, solution (A) containing the desired amount of metal (Cu, Mg and Al) nitrates and solution (B) containing the precipitating agents (i.e., $NH_4OH$ and $Na_2CO_3$) were added slowly and simultaneously into a beaker containing distilled water, while maintaining the pH constant at around $10 \pm 0.1$ with vigorous stirring at 50 °C to obtain the precipitate. The precipitate was filtered and washed with distilled water five times. The precipitate was then dried in air at 100 °C for 24 h.

### 2.2. Characterization of the catalysts

The chemical analyses of the prepared hydrotalcites were characterized by inductively coupled plasma-atomic emission spectroscopy (ICP-AES) with Varian Vista-Pro Axial using a simple solution calibration, where they were dissolved in 50% $HNO_3$. C, H and N concentrations were determined from 5 to 20 mg of solid samples on a CHN Elemental Analyzer. Scanning Electron Microscopy–energy dispersive X-ray spectrometer) (SEM–EDX) measurements were carried out using a JEOL JSM840A fitted with an Oxford Instruments INCA energy dispersive analytical system. Coating of each of the powder was attached to an aluminum block using double sided carbon tape. SEM images (20×) were acquired of each of the powders and EDX analysis of 3 points of each sample was performed. X-ray Diffraction (XRD) patterns were obtained using Bruker D8 advance target diffractometer. The patterns were run with copper Kα with secondly monochromator (λ = 1.5405 Å) at 40 kV and 40 mA. The crystallite size of hydrotalcite phases was calculated using Scherrer equation: $D = B\,\lambda/\beta_{1/2}\cos\Theta$; where $D$ is the average crystallite size of the phase under investigation, $B$ is the Scherrer constant (0.89), λ is wavelength of the X-ray beam used, $\beta_{1/2}$ is the full width at half maximum (FWHM) of diffraction peak and $\Theta$ is the diffraction angle.

Textural properties (BET-surface area, micropore area, pore size, total pore volume) were determined from nitrogen adsorption/desorption isotherms at −196 °C using a model Tristar 3000 automated gas sorption system (Micromeritics, USA). Continuous-wave (cw) electron spin resonance spectroscopy (ESR) experiments were performed at 30 K on a Bruker EMXplus spectrometer operating at 9.4 GHz equipped with a 4122SHQE resonator and an Oxford Instruments ESR900 cryostat. All measurements were carried out with 0.2 mW microwave power, 100 kHz modulation frequency, 0.1 mT modulation amplitude and 10 ms conversion time and time constant. FTIR spectra were recorded on a Perkin–Elmer Spectrum 100 FTIR spectrometer using KBr pellets (1 wt.% sample in KBr matrix). The X-ray photoelectron spectroscopy (XPS) measurements were carried out by using a SPECS GmbH X-ray

photoelectron spectrometer. Prior to analysis, the samples were degassed under vacuum inside the load lock for 16 h. The binding energy of the adventitious carbon (C *1s*) line a 284.6 eV was used for calibration, and the positions of other peaks were corrected according to the position of the C *1s* signal. The $H_2$ TPR, $CO_2$ TPD analyses were performed using CHEMBET 3000, Quantachrome, USA.

### 2.3. Typical procedure for Ullmann condensation reaction

#### 2.3.1. Microwave irradiation

The reaction using microwave irradiation was carried out using CEM Discover Labmate™ microwave apparatus (300 W with ChemDriver™ Software). The catalyst (0.5 g), in absence or presence of KOH or $K_2CO_3$ (2.0 mmol), iodobenzene (1) (2.0 mmol) and DMSO (4.0 mL) were mixed in a glass process vial. The vial was capped tightly and it was irradiated with microwaves with power of 300 W to reach a reaction temperature of 120 °C under auto generated pressure. The vial was exposed to microwaves for a required time to complete the reaction. The progress of the reaction was monitored by thin layer chromatography (TLC) for every 4 min (eluent; petroleum ether: chloroform). Upon completion of the reaction, the catalyst was removed by filtration and washed with $CHCl_3$ solvent and the solvent was evaporated under reduced pressure to obtain the product.

#### 2.3.2. Conventional electrical heating method

For comparison, the reactions were performed on the same scale as described above and carried out using conventional chemistry methodology. The reactants and catalyst were put in a flask. The reaction mixture was heated at 120 °C in a thermostatic oil-bath for required time to complete the reaction as monitored by TLC. After the completion of the reaction, the reaction mixture was cooled to room temperature and the products were obtained as described in the previous method.

### 2.4. Analyses of the reaction products

All melting points were measured on a Gallenkamp melting point apparatus and are uncorrected. The infrared spectra were recorded in KBr disks on Shimadzu FTIR 8101 PC infrared spectrophotometers. The NMR spectra were recorded on a Varian Mercury VX-300 NMR spectrometer. $^1H$ spectra were run at 300 MHz in $CDCl_3$. Chemical shifts were related to that of the solvent. GC–MS analysis was carried out using Shimadzu, GCMSQP2010S equipped with a direct insertion probe (DIP) was used to acquire the mass spectra of extracted volatile organic compounds and detected in the electron impact mode (EI–MS) by the application of 70 eV as the ionization energy.

## 3. Results and discussion

### 3.1. Ullmann homocoupling of iodobenzene

All the samples have been tested as catalysts for the classic Ullmann homocoupling of iodobenzene reaction (Scheme 2) without using any base via conventional means and microwave irradiation.

The catalytic activity data of the catalysts is tabulated in Table 1. The MgLDH sample was virtually non-active under both conventional and microwave conditions. In contrast, CuLDH-1 CuLDH-2 and CuLDH-3 catalysts showed substantial activity, the maximum biphenyl yield for the reaction ca. 54%, 77% and 91% respectively under microwave irradiation and 69%, 72% and 89% respectively under conventional heating. The dehalogenation product benzene is the only detected byproduct under the studied reaction conditions. The main advantage of microwave heating over the conventional heating is that it needed only 12–20 min while conventional heating required 10 h to obtain consider good biphenyl yield.

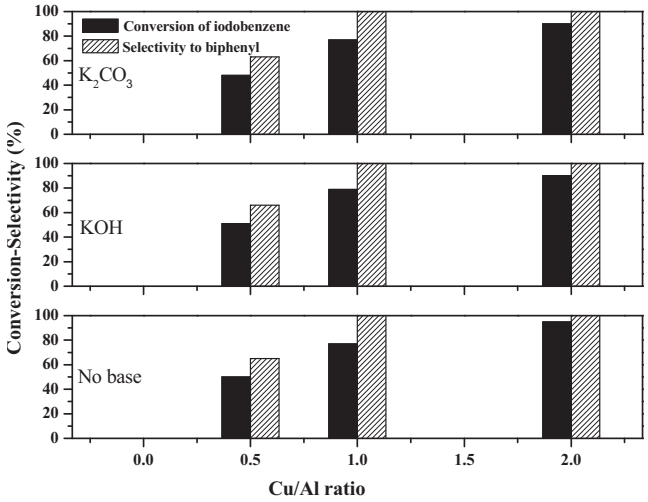


**Fig. 1.** Catalytic performance of hydrotalcite catalysts using $K_2CO_3$, KOH and no base.

It is clear from results cited in Table 1 that the best yields of the biphenyl using either microwave or conventional conditions were achieved when the hydrotalcite catalyst containing the highest content of Cu (CuLDH-3) was used. Furthermore, when the microwave irradiation was used, the CuLDH-3 catalyst (where the Cu replaced all the Mg ions completely in the cationic sheet) showed very good efficiency over the Cu and Mg (CuLDH-1 and CuLDH-2) containing catalysts, since it gave the highest yield in the shortest reaction time.

To determine the effectiveness of hydrotalcite catalyst in the Ullmann homocoupling reaction, we performed the reaction under microwave conditions, by adding KOH and $K_2CO_3$ as additional base along with the catalyst. Fig. 1 shows the conversion of iodobenzene and selectivity to biphenyl over all the hydrotalcite samples. All the Cu containing hydrotalcite catalysts offered almost similar catalytic activity in presence or absence of base. These results indicate that the Cu containing hydrotalcite is not only catalyzing the reaction, but also acting as a base. It is also worth noting that the MgLDH sample did not provide any catalytic activity even though it contained same interlayer anions as Cu containing hydrotalcites. This observation suggests that Cu ions are necessary for the Ullmann homocoupling reaction.

The scope and generality of this protocol was tested for bromobenzene, chlorobenzene and other derivatives of iodobenzene as shown in the Scheme 2 using highly active CuLDH-3 catalyst under the same reaction conditions listed in experimental section and corresponding biphenyl derivatives were obtained in good yield (Tables 2 and 3).

As shown in Table 2, the electron-rich aryl iodides (entry 3 and entry 4) were homocoupled at a much higher conversion (95%) than the electron-deficient 1-iodo-4-nitrobenzene (75%, entry 5). In general, the reaction gave very good yields and was highly successful for iodides and bromides. Activity has been lowered for chlorides.

In order to show the significance of this work, we compared the catalytic activity of CuLDH-3 in Ullmann homocoupling reaction with reported heterogeneous catalysts in the literature.

Table 6 shows experimental conditions and results found in the literature for different heterogeneous catalysts. Comparing our best catalyst, we can state that our catalyst is more reactive, considering that the Cu–Al LDH is stable, cheaper, highly active and that the reaction temperature is either lower or the reaction time shorter.

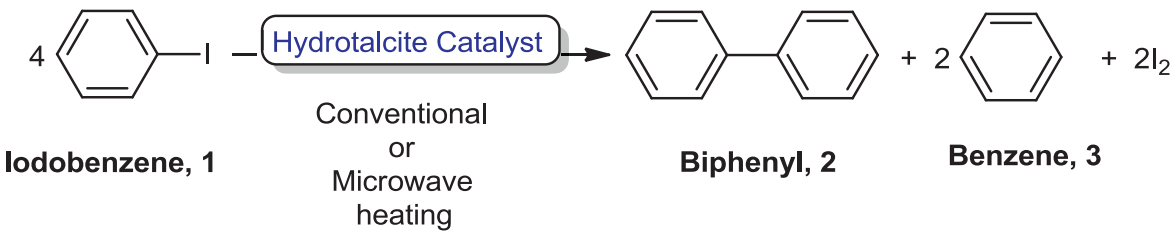


**Scheme 2.** Ullmann homocoupling of iodobenzene.

**Table 1**
Catalytic performance of hydrotalcite catalysts under microwave and conventional heating methods.

| Catalyst | Microwave irradiation[a] | | | | Conventional heating[a] | | | |
|---|---|---|---|---|---|---|---|---|
| | Time (min) | Conversion (%) | Selectivity (%) | Yield[b] (%) | Time (h) | Conversion (%) | Selectivity (%) | Yield[b] (%) |
| MgLDH | 60 | 0 | 0 | 0 | 24 | 0 | 0 | 0 |
| CuLDH-1 | 20 | 63 | 85 | 54 | 10 | 89 | 100 | 69 |
| CuLDH-2 | 15 | 77 | 100 | 77 | 10 | 74 | 97 | 72 |
| CuLDH-3 | 12 | 91 | 100 | 91 | 10 | 89 | 100 | 89 |

[a] Iododbenzene (1) (2.00 mmol), hydrotalcite catalyst (1.25 g), DMSO (4 mL), reaction temperature; 120 °C.
[b] Isolated yields of biphenyl (2).

**Table 2**
Ullmann homocoupling of aryl iodides using CuLDH-3 catalyst under microwave irradiation.

| Entry | Substrate[a] | Time (min) | Conversion (%) | Selectivity to biphenyl derivative (%) |
|---|---|---|---|---|
| 1 | 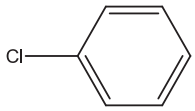 | 10 | 85 | 95 |
| 2 | 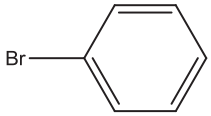 | 10 | 95 | 95 |
| 3 | 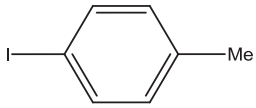 | 10 | 95 | 98 |
| 4 | 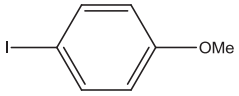 | 10 | 95 | 98 |
| 5 | 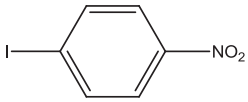 | 10 | 75 | 90 |

[a] Substrate (1) (2.00 mmol), hydrotalcite catalyst (1.25 g), DMSO (4 mL), reaction temperature; 120 °C.

### 3.2. Chemical analysis

Chemical analyses of the dried hydrotalcite catalysts were carried out using an ICP-AES technique. The atomic percentages of Cu, Mg, Al, C, H, N elements and Cu/Al and Mg/Al atomic ratios of the hydrotalcite compounds are shown in Table 4. Detailed characterizations of the fresh catalysts were performed to understand how the structure of hydrotalcite and Cu ions are playing the role in reaction Ullmann homocoupling reaction mechanism.

The atomic composition results obtained from EDX analysis were similar and in accordance with this data. The actual Cu, Mg and Al species contents analyzed in the solids were very similar to nominal contents indicating the efficiency of the preparation method.

**Table 3**
Comparison of CuLDH-3 activity with heterogeneous catalysts reported in the literature.

| References | Catalytic system | Reaction conditions | Conv. iodobenzene (%) | Sel. biphenyl (%) |
|---|---|---|---|---|
| Wan et al. [15] | Pd/Ph-MCM-41 | $H_2O$, KOH, HCOONa, 100 °C, 10 h | 75.5 | 98 |
| Samim et al. [20] | Cu nanoparticles (5 nm) | DMSO, 200 °C, 5 h | 95 | 100 |
| Li et al. [24] | $Au_{25}(SR)_{18}/CeO_2$ | DMF, $K_2CO_3$, 130 °C, 48 h | 99.8 | 100 |
| Ponce & Klabunde [19] | Cu nanoparticles | Toluene, 150 °C, 6 h | 89 | 100 |
| Present work | CuLDH-3 | DMSO, 120 °C, microwaves, 12 min | 91 | 100 |

**Table 4**
Chemical analysis of hydrotalcite samples.

| Catalyst | C | H | Cu | Mg | Al | Cu/Al | Mg/Al |
|---|---|---|---|---|---|---|---|
| MgLDH | 3.26 | 4.07 | 0.0 | 20.7 | 10.3 | 0.0 | 2.00 |
| CuLDH-1 | 2.85 | 3.29 | 5.4 | 15.5 | 10.1 | 0.53 | 1.53 |
| CuLDH-2 | 2.88 | 3.86 | 10.9 | 10.4 | 10.7 | 1.01 | 0.97 |
| CuLDH-3 | 1.80 | 2.75 | 23.1 | 0.0 | 12.0 | 1.92 | 0.0 |

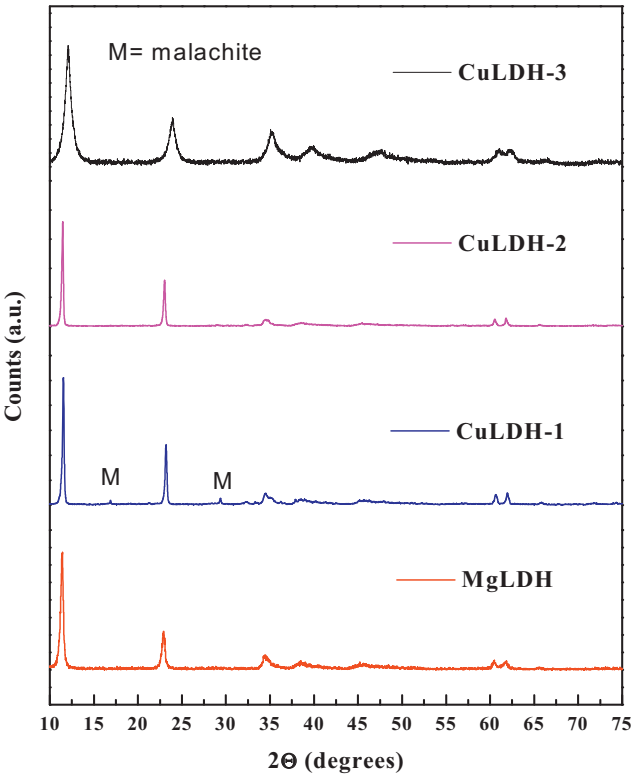


**Fig. 2.** XRD patterns of as-synthesized hydrotalcite samples.

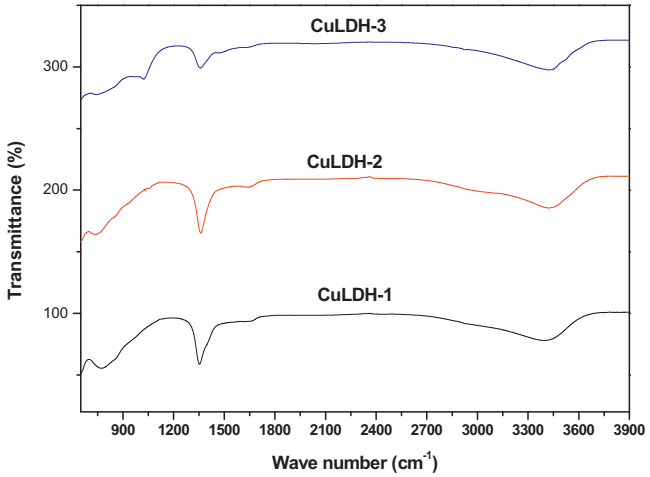


**Fig. 3.** FTIR spectra of CuMgAl hydrotalcites.

### 3.3. Powder X-ray diffraction (XRD)

The XRD patterns of the as-synthesized hydrotalcite samples are shown in Fig. 2. All the samples showed diffraction peaks at $2\theta = 11^\circ, 24^\circ, 35^\circ, 38^\circ, 46^\circ$, and $60^\circ$ ascribed to diffraction by basal planes (0 0 3), (0 0 6), (1 0 5), (1 0 8), (0 0 9) and (1 1 0), respectively. These are the typical diffraction patterns of hydrotalcite-like materials [JCPDS 22-0700] having layered structure with intercalated carbonate anions [30]. A hydrotalcite phase was only detected in MgLDH and CuLDH-3 samples. A small amount of malachite phase [$Cu_2(OH)_2CO_3$, JCPDS 10-0399] appeared in the XRD patterns of CuLDH-1 and CuLDH-2 samples. Hence, it appears that there is a limitation on the amount of Cu incorporation in the Mg–Al hydrotalcite framework.

This result indicates that under the adopted preparation conditions, less than 16.6% atomic ratio of Mg ions can be isomorphously substituted by Cu in the Mg–Al brucite layer to obtain pure and homogeneously dispersed Cu–Mg–Al HT sample. Jiang et al. [31] reported that the Jahn-Teller distortion of Cu in octahedral coordination could be the reason for lower stability of the Cu hydrotalcite phase and its subsequent formation of malachite. No significant positional changes in the basal plane reflections were observed with the variation in the Cu/Mg atomic ratio. This may be due to a small difference in the octahedral ionic radii of $Cu^{2+}$ (0.73 Å) and $Mg^{2+}$ (0.72 Å). However, the Cu content influenced the crystallinity of the Cu–Mg–Al hydrotalcite samples, which can be seen from both XRD patterns (Fig. 2) and structural parameters (Table 5). MgLDH, CuLDH-1, CuLDH-2 samples are highly crystalline and the crystallanity of the samples is increasing with the increase of Cu content. In contrast, the CuLDH-3 showed much lower crystallanity than the Mg containing samples.

The average crystallite sizes in *a* direction were calculated from (0 0 3) plane using Debye–Scherrer equation and summarized in Table 5. The crystallite sizes of the HT samples varied in the range 16–35 nm. The CuLDH-3 sample, with the largest Cu content in a single hydrotalcite phase, exhibits the smallest crystallite size at about 16 nm. The lattice parameters of all the MgLDH, CuLDH-1 and CuLDH-2 samples are similar. This confirms the uniform substitution of $Cu^{2+}$ ions to $Mg^{2+}$ ions in the cationic sheets of CuLDH-1 and CuLDH-2 samples. The lattice parameters of CuLDH-3 sample were smaller, which indicates that the removal of Mg from the hydrotalcite structure decreases the lamellar spacing.

### 3.4. FTIR spectroscopy

The FTIR spectra of Cu incorporated hydrotalcites are presented in Fig. 3. All the samples exhibited characteristic broad absorption band centered at 3420 $cm^{-1}$, due to presence of interlayer $H_2O$ molecules and structural hydroxyl groups in the brucite layer. The weak peak at 1640 $cm^{-1}$ is attributed to an interlayer $H_2O$ bending vibration and a strong peak at 1350 $cm^{-1}$ results from the $\nu_3(CO_3^{2-})$ antisymmetric stretching mode [25]. Another small band at 875 $cm^{-1}$ can be observed in all the samples and is assigned to an out-of-plane deformation in the $\nu_4$ mode of carbonate ion [32].

It was reported [33] that in the FTIR spectrum of malachite each of the six non-degenerate modes of the $CO_3^{2-}$ ion, could split into two IR active components (particularly in the region of 1520–1390 $cm^{-1}$ that are attributed to the $\nu_3$ mode of the carbonate ion) under $C_{2h}$ symmetry, as a result of the correlation field splittings. However, the FTIR spectra of CuLDH-1 and CuLDH-2 samples did not show any such peaks with splittings, even though XRD results showed that these two samples contained small of amount of malachite phase.

**Table 5**
Crystallographic data from XRD patterns and textural properties of hydrotalcite samples from $N_2$ physisorption.

| Catalyst | Lattice parameters (Aº) | Crystallite size (nm) | $S_{BET}$ ($m^2$/g) | $V_p$ ($cm^3$/g) | $D_p$ (nm) |
|---|---|---|---|---|---|
| MgLDH | $a$ = 3.068, $c$ = 22.830 | 38.00 | 90 | 0.7420 | 20 |
| CuLDH-1 | $a$ = 3.068, $c$ = 22.830 | 30.73 | 73 | 0.4068 | 10 |
| CuLDH-2 | $a$ = 3.068, $c$ = 22.830 | 29.59 | 75 | 0.2614 | 15 |
| CuLDH-3 | $a$ = 3.050, $c$ = 23.120 | 16.07 | 30 | 0.1001 | 45 |

$S_{BET}$: specific BET surface area; $V_p$: total pore volume; $D_p$: average pore diameter.

A major spectral change was noticed in the FTIR spectrum of CuLDH-3 sample (Fig. 3) showing a new band at 1045 $cm^{-1}$. The peak at 1045 $cm^{-1}$ could be identified as an unperturbed $CO_3^{2-}$ $\nu_1$ symmetric stretching vibration; this peak is not presented in either the CuLDH-1 and CuLDH-2 spectra. This observation suggests that two different types of $CO_3^{2-}$ ions are presented in the CuLDH-3 sample. It is possible that these new carbonate species might be isolated metal carbonates.

### 3.5. Nitrogen gas physisorption

Nitrogen gas adsorption–desorption isotherms at −196 °C for all the samples are shown in Fig. 4. All the samples show the type II pattern based on the Brunauer, Deming, Deming and Teller (BDDT) classification [34] with a type B hysteresis loop, the area of which increased with increasing Cu/Al ratio from 0 (MgLDH) to 0.5 (CuLDH-1). Increasing the Cu/Al ratio further to 1 (CuLDH-2) and 2 (CuLDH-3), caused a decrease in the area under hysteresis loop.

The hysteresis loops are at a relative pressure of 0.5–1.0 for MgLDH and CuLDH-1 samples indicating pore architecture of large mesoporous dimensions. CuLDH-2 and CuLDH-3 samples have hysteresis loops at relative pressures of 0.6–1.0 revealing that the interlayer space is inaccessible for nitrogen molecules. These results are further corroborated by the pore size distribution of these samples, shown as an inset in Fig. 4.

It is known that the distribution of pores in hydrotalcites is influenced by the crystallite size and packing arrangement of crystallites [35]. A relatively narrow distribution of pores was observed for MgLDH and CuLDH-1 samples, whereas a broader distribution of pores can be observed for CuLDH-2 and CuLDH-3 samples. This is indeed reflected in the BJH pore diameter of these samples (plotted from the desorption branch of the isotherm). The textural properties of all the samples are tabulated in Table 5. The average pore diameter of MgLDH sample is around 20 nm, in contrast the CuLDH-3 sample showed 45 nm, and with the specific surface area of the former was twice that of the latter. The specific surface area, total

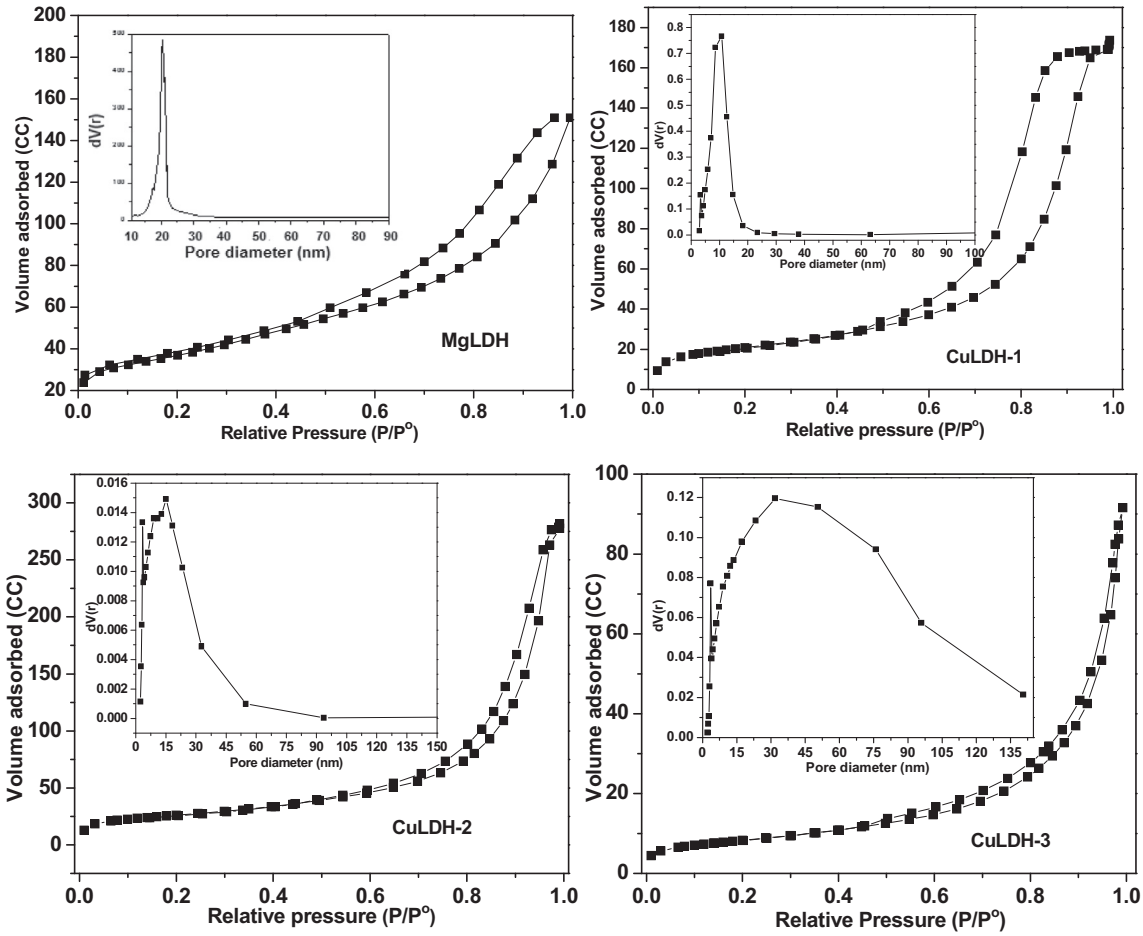


**Fig. 4.** Adsorption–desorption isotherm (inset: BJH pore size distribution) of hydrotalcite samples.

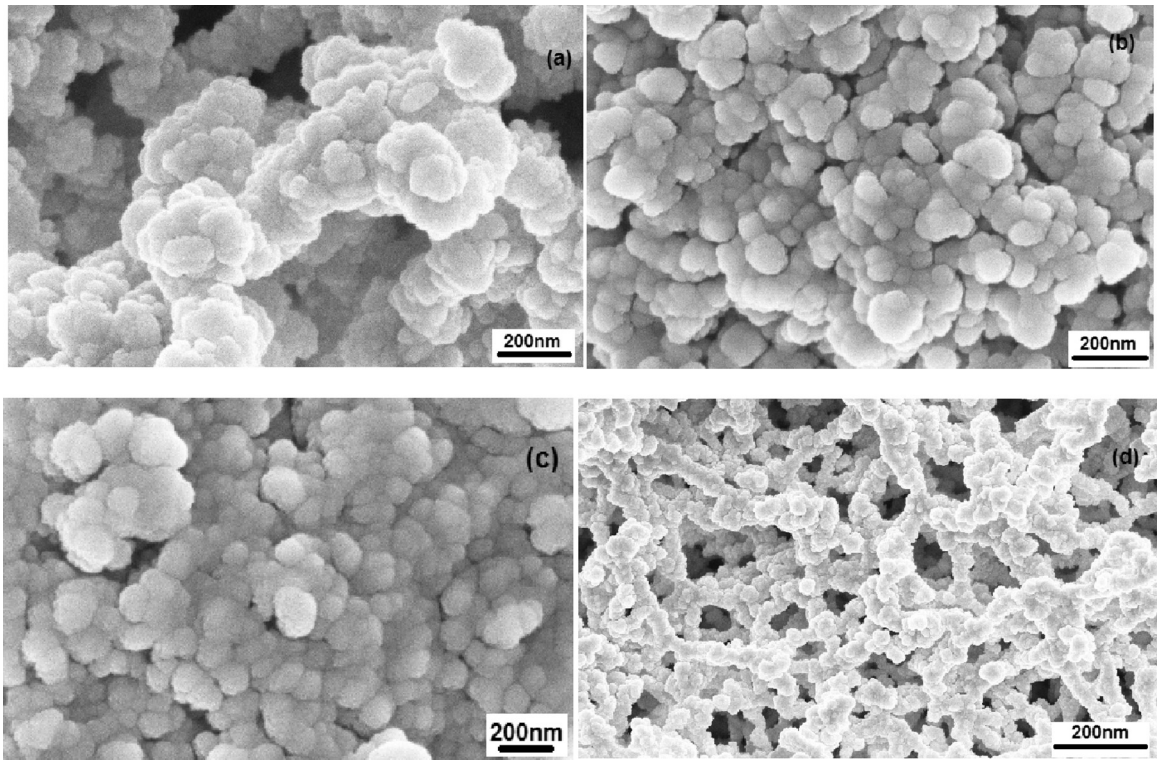


**Fig. 5.** SEM images of (a) MgLDH (b) CuLDH-1 (c) CuLDH-2 and (d) CuLDH-3.

pore volume and the area of the hysteresis loop decreased with an increase in Cu content. These changes probably originate from morphological differences in the crystallites arising with a change in Cu and Mg concentration.

### 3.6. Scanning electron microscopy (SEM)

SEM was used to study the morphology of these samples to get more information about the arrangement of crystallites in these samples. The SEM images of MgLDH, CuLDH-1, CuLDH-2 and CuLDH-3 are shown in Fig. 5. The crystallites in all the samples are clumped together, poorly dispersed and exhibiting spongy type of morphology. The crystallites are ambiguous in appearance and lack distinct particle edges, particularly in the CuLDH-1 and CuLDH-2 samples. The crystallite particles in MgLDH and CuLDH-3 samples were arranged in semi-hexagonal shape to create inter-particle channels.

The extent of agglomeration appears to be decreasing with increase of Cu content. In MgLDH sample, the crystallites agglomeration occurs strongly in forming such spongy particles 30–40 nm in diameter, whereas CuLDH-3 consists of particles of 20–25 nm. This is in accordance with XRD and pore size distribution results where contributions of larger pores were formed in greater numbers through interparticles for CuLDH-3 sample.

### 3.7. Electron spin resonance spectroscopy (ESR)

To determine the electronic properties of Cu species in the samples. Fig. 6 shows the ESR spectra for CuLDH-1, CuLDH-2 and CuLDH-3 samples.

MgLDH sample is ESR inactive. The ESR signals of Cu incorporated samples are anisotropic with clearly defined $g_{||}$ and $g_{\perp}$ regions as expected for $Cu^{2+}$ in a surrounding of axial symmetry. The spectral parameters can be interpreted as arising from distorted octahedrally coordinated $Cu^{2+}$ ions [36].

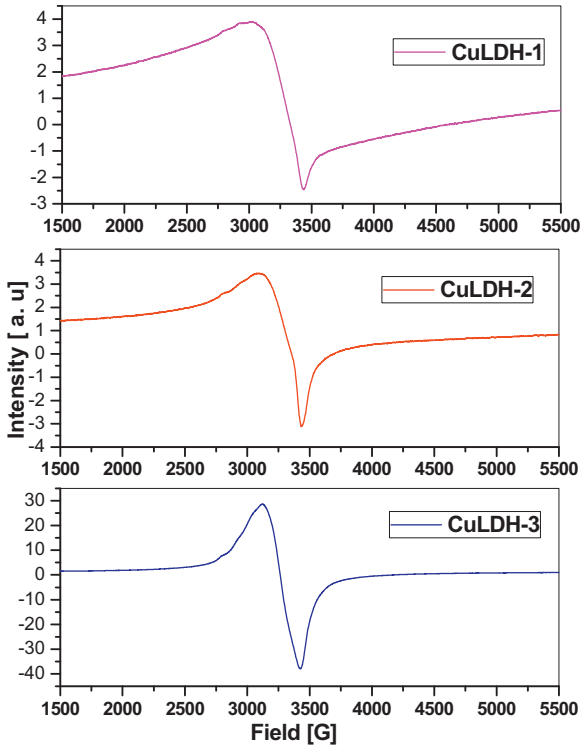


**Fig. 6.** ESR spectra of Cu incorporated samples.

According to Bahranowski et al. [37], appearance of well-resolved ESR signals means that $Cu^{2+}$ ions are uniformly dispersed in the LDH structure surface. The higher the Cu concentration the broader the ESR signal. CuLDH-1, which has the lower Cu-content (5.1%) shows the sharpest peak. CuLDH-2 and CuLDH-3, with a

higher Cu-content (10.9% and 23.1% respectively) in comparison with CuLDH-3, shows broader ESR signal.

The broad line width with the increase of Cu-content can be attributed to dipolar broadening effects caused by mutual interactions between paramagnetic $Cu^{2+}$ ions, indicating that the corresponding ions were located in a $Cu^{2+}$ containing aggregated phase of clusters [38]. The presence of Cu contained clusters in different concentration on three catalysts lead to the difference of ESR signal. It was clear that more Cu contained clusters appeared on catalyst CuLDH-3 than CuLDH-2 and CuLDH-1.

### 3.8. X-ray photoelectron microscopy (XPS)

To gain further insight into the location and nature of the Cu species present in these samples, XPS investigation was undertaken. Deconvoluted Cu $2p_{3/2}$ X-ray photoelectron spectra for CuLDH-1, CuLDH-2 and CuLDH-3 samples are shown in Fig. 7. It was reported that binding energy in the range of 933.0–933.8 eV for the Cu$2p_{3/2}$ peak and shake-up peaks are characteristic for CuO, while binding energy of 932.2–933.1 eV and absence of shake-up peaks is characteristic for $Cu_2O$ [39]. All Cu incorporated samples exhibited principle Cu $2p_{3/2}$ broad profile consisted of two peaks in between 930 eV and 938 eV, which could be attributed to $Cu^{2+}$ species [40]. The peaks have been deconvoluted into two contributions with binding energies centered at 932.8 eV and 934.9 eV respectively. The former peak can be assigned to isolated $Cu^{2+}$ species [41] and the latter maybe related to another state where Cu ions coordinate with Mg and Al in a spinel like species. Quantification of Cu ions presented in Cu LDH samples was performed (Table 6). It is interesting to note that the CuLDH-3 sample contained the highest amount of isolated $Cu^{2+}$ species (65%).

### 3.9. $H_2$-temperature programmed reduction ($H_2$-TPR)

$H_2$-TPR was used to investigate the reducibility of the samples and to understand contribution made by different copper species found in these materials. The $H_2$-TPR patterns of all the samples are shown in Fig. 8.

The MgLDH sample showed three reduction peaks with the major peak at 550 °C. Two small peaks at 300 °C and 425 °C are assigned to the reduction of a small amount of impurities remaining in the solid from the raw materials. The major peak at 550 °C may be due to the reduction of $Mg^{2+}$ ions. With the gradual replacement of Mg for Cu cations, new peaks can be identified in the overall TPR patterns. Broad peaks in the temperature range of 200–400 °C can be observed for the CuLDH-1 sample and these peaks can related to the reduction of $Cu^{2+}$ cations, which also include isolated copper ions, weak magnetic associates, and small two- and three-dimensional clusters [42].

Nagaraja et al. [43] observed two broad peaks at high temperature, ranging from 300 °C to 560 °C, they suggested that these peaks are possibly due to the reduction of Cu ions that are strongly associated with hydrotalcite. The peak at 650 °C can be ascribed to the reduction of bulky CuO phases that include large clusters. Isolated Cu ions can react easily with other components of the sample and form various surface Cu components of different reducibility [44]. With the increase of Cu content, the reduction peaks shifted toward low temperatures and multiple weak peaks were transformed into a single intense peak – as can be observed in the CuLDH-2 sample. This observation could infer an enhancement of reducibility of the catalyst, with rapid reduction of Cu ions. Agrell et al. [45] stated that the shift in the reduction temperature peak in the TPR patterns of Cu–Zn–Al oxide catalysts is due to the presence of larger CuO crystallites.

The hydrogen consumption value of CuLDH-3 (328 μmol $g^{-1}$) is higher than CuLDH-2 (284 μmol $g^{-1}$ and CuLDH-1 (245 μmol $g^{-1}$).

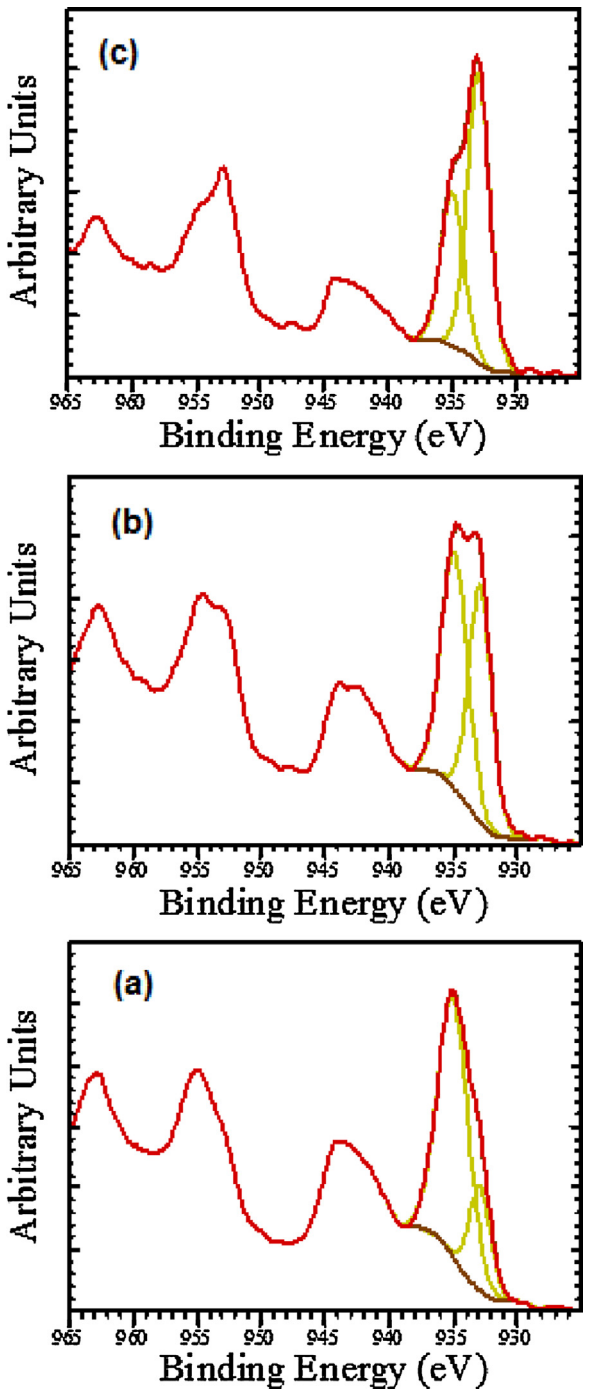


**Fig. 7.** Deconvoluted Cu $2p_{3/2}$ XPS spectra for CuLDH-1, CuLDH-2 and CuLDH-3 samples.

A higher amount of Cu cations (CuLDH-3) in the hydrotalcite causes an increase in the portion of easily reducible copper particles, showing a reduction peak at temperatures lower than 400 °C. This trend is similar to that described in the catalytic test, suggesting that the catalytic activity is related to the amount of Cu ions that are easily reducible. Very similar $H_2$-TPR profiles for CuO supported on $Al_2O_3$ has been reported by other authors and they indicated that the redox properties of the catalysts were influenced by the interaction of Cu ions with $Al_2O_3$ support and small Cu cluster and/or isolated $Cu^{2+}$ ions are reduced at lower temperature than Cu larger/cluster particles [46]. From these observations, we can state that a low concentration of Cu and a high concentration of Mg in LDH materials

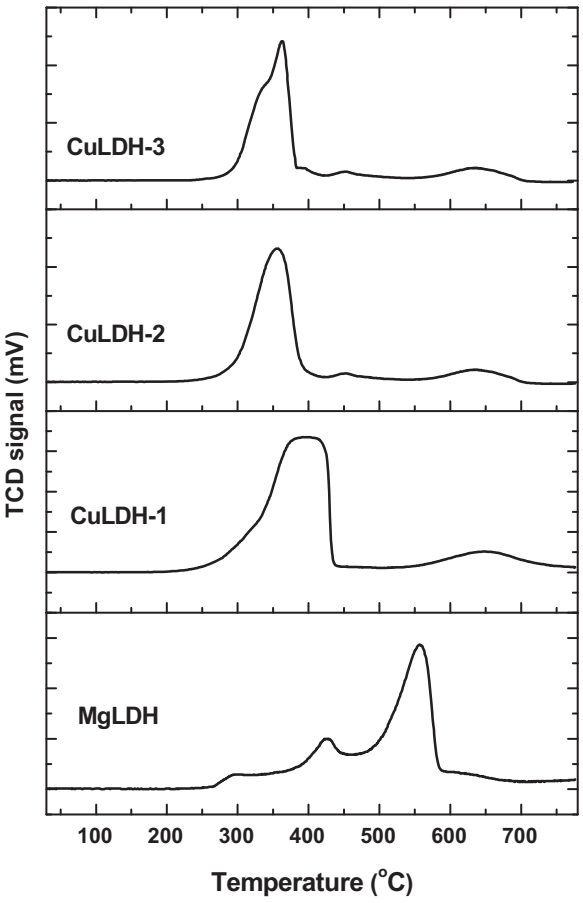


**Fig. 8.** $H_2$ TPR patterns of hydrotalcite samples.

led to deterioration of the reducibility of the Cu(II) component in the solids and as a consequence decrease of catalytic activity was noticed.

It is evident from characterization results that the CuLDH-3 showed its unique characteristics from the CuLDH-1 and CuLDH-2 catalysts and CuLDH-3 was also more active. This is a somewhat expected result and can be explained using the physicochemical data. An increase in Cu content resulted in increased contribution from the isolated Cu species. Reduction of pore volume, due to the filling of interlayer space with Cu species, was observed with the increase of Cu content; however, the increase of pore diameter due to the formation of semi-hexagonal interparticle channels made active phase accessible to the reagents.

XPS analysis of Cu incorporated samples revealed that Cu species distribution is different for each sample (Table 6). The area under the two $2p_{3/2}$ peaks has been quantified for three samples and the corresponding percentages have been calculated as a function of the total area of the peaks.

In the Fig. 9, the percentages of isolated $Cu^{2+}$ ions are drawn against the Cu/Al ratio and conversion of iodobenzene. As we can observe, CuLDH-3 possessed highest contribution of most reduced

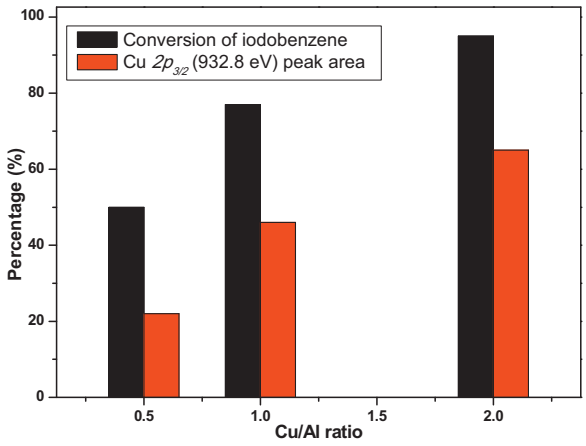


**Fig. 9.** Correlation of Cu/Al ratio with Cu $2p_{3/2}$ peak area percentage and conversion of iodobenzene.

$Cu^{2+}$ species, with 65% of isolated $Cu^{2+}$ species appearing with binding energy at 932.8 eV offering highest conversion of iodobenzene.

$H_2$-TPR data revealed that higher amount of Cu cations in the hydrotalcite layers led to an increase of the portion of easily reducible copper particles, which are active species for C—C coupling reactions. Isolated Cu ions that might be diluted (separated) by the high Mg-content, might improve the selectivity to desired product, avoiding the further reaction of the desired product (i.e., avoiding the formation of by products).

### 3.10. Ullmann homocoupling reaction mechanism over Cu hydrotalcites

The mechanistic pathways of Ullmann homocoupling of iodobenzene over Cu–Mg–Al hydrotalcite can be depicted as shown in Fig. 10. For this catalytic cycle, the nucleophile species in the hydrotalcite framework ($OH^-$) reacts with the Cu(II) species followed by an oxidative addition of the iodobenzene molecule to Cu(II) to form the Cu(III) intermediate. Subsequently, the iodide on Cu is exchanged for the nucleophile and the obtained intermediate, via a reductive elimination step, releases the coupling product and the active Cu(II) catalyst is regenerated.

In a recent review, Sperotto et al. [47] mentioned that pinpointing an individual Cu oxidation state involved in Ullmann coupling reaction is difficult, since Cu is likely to be present at more than one oxidation level, proportions of which may alter during the reaction as a result of redox processes. It is also interesting to note that the MgLDH sample without any Cu in the framework is completely inactive for this reaction even though it possessed stronger basic sites than Cu doped catalysts [48]. This indicates that easily reducible Cu species are enhancing the redox cycle, which is crucial for achieving high conversion and yields.

### 3.11. Reusability of Cu hydrotalcite catalyst

The reusability of the CuLDH-3 catalyst was determined over several reaction cycles under optimized reaction conditions. The

**Table 6**
Quantification of Cu species presented in the samples by XPS analysis and $H_2$ consumption values from TPR measurements.

| Sample | H2 consumed during TPR (μmol $g^{-1}$) | $Cu^{2+}$ isolated species Sample | | $Cu^{2+}$ cluster species during TPR | |
|---|---|---|---|---|---|
| | | Binding energy (eV) | Percentage | Binding energy (eV) | Percentage |
| CuLDH-1 | 245 | 932.8 | 22 | 934.9 | 78 |
| CuLDH-2 | 284 | 932.8 | 46 | 934.8 | 54 |
| CuLDH-3 | 328 | 932.8 | 65 | 934.9 | 35 |

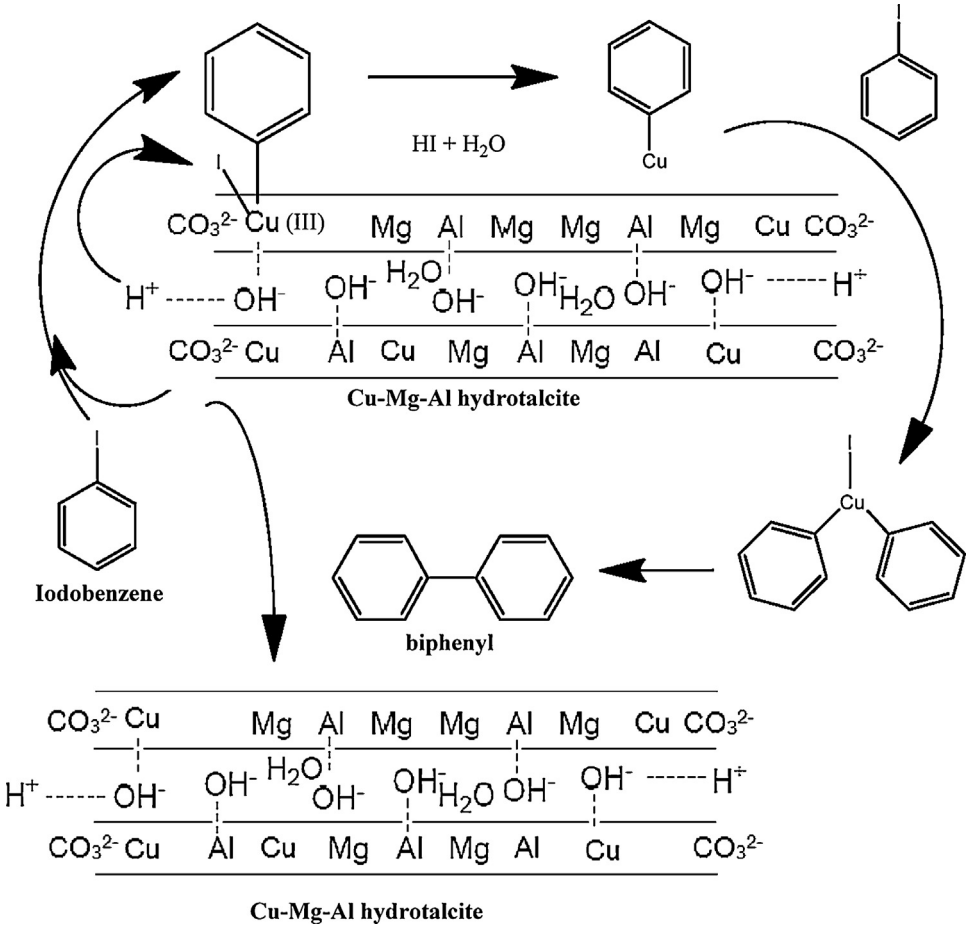


**Fig. 10.** Plausible mechanism of Ullmann homocoupling of iodobenzene over Cu–Mg–Al hydrotalcite.

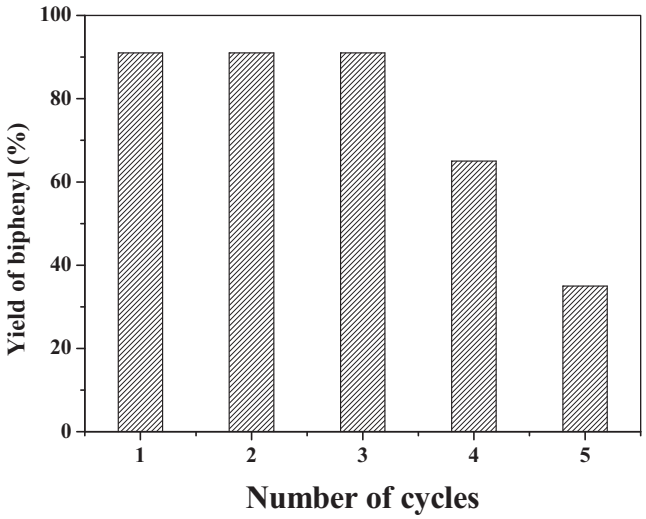


**Fig. 11.** Reusability of CuLDH-3 catalyst.

reactivation of the catalyst was carried out by heating the recovered solid in an oven for 2 h at 60 °C.

As can be seen in Fig. 11, a constant activity of the catalyst was observed until the third regeneration cycle. However, a decrease in the yield of biphenyl was observed in the fourth cycle. In the fourth regeneration cycle, the yield fell from 91% to 65%. In the fifth regeneration cycle, the yield was only of 35%. The pronounced decay in the catalytic activity may be attributed to the possible pore blocking and the loss of catalyst during the reaction and regeneration processes.

## 4. Conclusions

In summary, Cu–Mg–Al hydrotalcites with different Cu:Mg:Al atomic compositions were successfully synthesized. The synthesized materials were applied as catalysts for an Ullmann homocoupling reaction under microwave irradiation without using any base or reducing agent. The coupling of both electron-rich and electron-poor aryl halides was facilitated in the protocol. Microwave irradiation was shown to be rapid and more efficient than conventional heating methods to produce biphenyl derivatives. Activity for the Ullmann homocoupling of aryl iodides reaction increased with increasing Cu concentration. Maximum activity was found for the catalyst that contained an atomic ratio of Cu/Al = 2, Mg/Al = 0 (CuLDH-3). Variation in the catalytic activity was due to varied phase compositions (influenced by the Cu/Mg atomic ratio, as indicated by XRD, FTIR). The better intrinsic activity for the CuLDH-3 sample with a high copper content was caused by several properties, including low crystallite size, high pore diameter and large amount of easily reducible isolated $Cu^{2+}$ species, and its facile redox behavior. The Cu contained hydrotalcite catalyst can be reused at least for three times without loss of activity.

## Acknowledgements

Authors thank Felicity Sartain, Milo S.P. Shaffer and Chris Kay for useful discussions, and Zlatko Saracevic (Department of Chemical

Engineering and Biotechnology, University of Cambridge, UK) for BET measurements. This project was funded by the Deanship of Scientific Research (DSR), King Abdulaziz University, Jeddah under Grant No. D-5/432. The authors, therefore, acknowledge DSR with thanks for their technical and financial support.

## Appendix A. Supplementary data

Supplementary data associated with this article can be found, in the online version, at http://dx.doi.org/10.1016/j.molcata.2013.08.013.

## References

[1] (a) R.F. Heck, Palladium Reagents in Organic Synthesis, Academic Press, London, 1985;
(b) A.M. Rosa, S. Prabhakar, A.M. Lobo, Tetrahedron Lett. 31 (1990) 1881–1884;
(c) M.A. Rizzacasa, M.V. Sargent, J. Chem. Soc.: Chem. Commun. (1990) 838–839;
(d) T. Yamato, C. Hideshima, G.K. Surya Prakash, G.A. Olah, J. Org. Chem. 56 (1991) 3192–3194.
[2] (a) A. de Meijer, F.E. Meyer, Angew. Chem. Int. Ed. Engl. 33 (1994) 2379–2411;
(b) I.P. Beletskaya, A.V. Cheperkov, Chem. Rev. 100 (2000) 3009–3066.
[3] J. Hassan, M. Sevignon, C. Gozzi, E. Schulz, M. Lemaire, Chem. Rev. 102 (2002) 1359–1469.
[4] M. Zeng, Y. Du, L. Shao, C. Qi, X.-M. Zhang, J. Org. Chem. 75 (2010) 2556–2563.
[5] (a) J. Papillon, E. Schulz, S. Gainas, J. Lessard, M. Lemaire, Synth. Met. 96 (1998) 155;
(b) S.S. Zhu, T.M. Swager, Adv. Mater. 8 (1996) 497–500.
[6] T. Yamamoto, T. Maruyama, Z. Zhou, T. Ho, T. Fukuda, Y. Yoneda, F. Begum, T. Ikeda, S. Sasaki, H. Takezoe, A. Fukuda, K. Kuhota, J. Am. Chem. Soc. 116 (1994) 4832–4845.
[7] G. Bringmann, R. Walter, R. Weirich, Angew. Chem. Int. Ed. Engl. 29 (1990) 977–991.
[8] J.M. Lehn, Supramolecular Chemistry, Ist ed., VCH, Verlasgesellschaft, 1995.
[9] Y. Chao, G.R. Weisman, G.D.Y. Sogah, D.J. Cram, J. Am. Chem. Soc. 101 (1979) 4948–4958.
[10] C.G. Bates, R.K. Gujadhur, D. Venkataraman, Org. Lett. 4 (2002) 2803–2806.
[11] Q. Zhang, D. Wang, X. Wang, K. Ding, J. Org. Chem. 74 (2009) 7187–7190.
[12] C. Wolf, S. Liu, X. Mei, A.T. August, M.D. Casimir, J. Org. Chem. 71 (2006) 3270–3273.
[13] Y. Pan, H. Lu, Y. Fang, X. Fang, L. Chen, J. Qian, J. Wang, C. Li, Synthesis (2007) 1242–1246.
[14] A.H.M. de Vries, J.G. de Vries, F.B.J. van Assema, B. de Lange, D. Mink, D.J. Hyett, P.J.D. Maas, WO 2006/069799.
[15] Y. Wan, J. Chen, D. Zhang, H. Li, J. Mol. Catal. A: Chem. 258 (2006) 89–94.
[16] D.A. Culkin, J.F. Hartwig, J. Am. Chem. Soc. 123 (2001) 5816–5817.
[17] T. Miao, L. Wang, Synthesis (2008) 363–368.
[18] T. Seshadri, A. Kettrupt, Z. Fresenius, Anal. Chem. 310 (1982) 1–5.
[19] A.A. Ponce, K.J. Klabunde, J. Mol. Catal. A: Chem. 225 (2005) 1–6.
[20] M. Samim, N.K. Koushik, A. Maitra, Bull. Mater. Sci. 30 (2007) 535–540.
[21] H.J. Cristau, P.P. Cellier, S. Hamada, J.F. Spindler, M. Taillefer, Org. Lett. 6 (2004) 913–916.
[22] A. Ouali, J.F. Spindler, H.J. Cristau, M. Taillefer, Adv. Synth. Catal. 348 (2006) 499–505.
[23] R.N. Jogdand, B.B. Shingate, M.S. Shingare, Tetrahedron Lett. 50 (2009) 4019–4021.
[24] G. Li, C. Liu, Y. Lei, R. Jin, Chem. Commun. 48 (2012) 12005–12007.
[25] F. Cavani, F. Triffiro, A. Vaccari, Catal. Today 11 (1991) 173–301.
[26] M. Leon, E. Diaz, S. Bennici, A. Vega, S. Ordonez, A. Auroux, Ind. Eng. Chem. Res. 49 (2010) 3663–3671.
[27] S.M. Auer, S.V. Gredig, R.A. Koppel, A. Baiker, J. Mol. Catal. 141 (1999) 193–203.
[28] K. Iwai, T. Yamauchi, K. Hashimoto, T. Mizugaki, K. Ebitani, K. Kaneda, Chem. Lett. 32 (2003) 58–59.
[29] (a) M. Mokhtar, T.S. Saleh, N.S. Ahmed, S.A. Al-Thabaiti, R.A. Al-Shareef, Ultrason. Sonochem. 18 (2011) 172–176;
(b) M. Mokhtar, T.S. Saleh, S.N. Basahel, J. Mol. Catal. A: Chem. 353/354 (2012) 122–131;
(c) T.S. Saleh, K. Narasimharao, N.S. Ahmed, S.N. Basahel, S.A. Al-Thabaiti, M. Mokhtar, J. Mol. Catal. A: Chem. 367 (2013) 12–22.
[30] M.V. Twigg, Appl. Catal. B: Environ. 70 (2007) 2–15.
[31] Z. Jiang, Z.P. Hao, J.J. Yu, H.X. Hou, C. Hu, Catal. Lett. 99 (2005) 157–163.
[32] R.L. Frost, A. Soisnard, N. Voyer, S.J. Palmer, W.N. Martens, J. Raman Spectroscop. 40 (2009) 645–649.
[33] D. Stoilova, V. Koleva, V. Vassileva, Spectrochim. Acta A 58 (2002) 2051–2059.
[34] O. Bergada, I. Vicente, P. Salagre, Y. Cesteros, F. Medina, J.E. Sueiras, Micropor. Mesopor. Mater. 101 (2007) 363–373.
[35] F. Prinetto, G. Ghiotti, P. Graffin, D. Tichit, Micropor. Mesopor. Mater. 39 (2000) 229–247.
[36] K. Bahranowski, M. Gasior, A. Kielski, J. Podobinski, E.M. Serwicka, L.A. Vartikian, K. Wodnicka, Clay Miner. 34 (1999) 79–87.
[37] K. Bahranowski, R. Dula, M. Gasior, M. Labanowska, A. Michalik, L.A. Vartikian, E.M. Serwicka, Appl. Clay Sci. 18 (2001) 93–101.
[38] J. Chen, Y. Zhan, J. Zhu, C. Chen, X. Lin, Q. Zheng, Appl. Catal. A: Gen. 377 (2010) 121–127.
[39] D. Brigs, M.P. Seah (Eds.), Practical Surface Analysis by Auger and X-ray Photoelectron Spectroscopy, Wiley, New York, 1983.
[40] R. Figueiredo, A.M. Arias, M.L. Granados, J.L. Fierro, J. Catal. 178 (1998) 146–152.
[41] F. Garbassi, G. Petrini, J. Catal. 90 (1984) 113–118.
[42] W.P. Dow, Y.P. Wang, T.J. Huang, Appl. Catal. A: Gen. 190 (2000) 25–34.
[43] B.M. Nagaraja, A.H. Padmasari, P. Seetharamulu, K. Hariprasad reddy, B. Davidraju, K.S. Ramarao, J. Mol. Catal. A: Chem. 278 (2007) 29–37.
[44] F. Severino, J. Brito, O. Carias, J. Laine, J. Catal. 102 (1986) 172–179.
[45] J. Agrell, H. Birgersson, M. Boutonnet, I.M. Cabrera, R.M. Navarro, J.L.G. Fiero, J. Catal. 219 (2003) 389–403.
[46] E. Moretti, M. Lenarda, L. Storaro, A. Talon, T. Montanari, G. Busca, E. Rodriguez, A. Jimeenez, M. Turco, G. Bagnasco, Appl. Catal. A: Gen. 335 (2008) 46–55.
[47] E. Sperotto, G.P.M. van Klink, G. van Koten, J.G. de Vries, Dalton Trans. 39 (2010) 10338–10351.
[48] Temperature programmed desorption (TPD) of $CO_2$ results; desorbed $CO_2$ amount ($\mu mol\ g^{-1}$) for MgLDH = 42.1, CuLDH-1 = 32.2, CuLDH-2 = 23.4, CuLDH-3 = 17.6.